Chemical Geology 622 (2023) 121386

Contents lists available at ScienceDirect

Chemical Geology

journal homepage: www.elsevier.com/locate/chemgeo

Geochemical features and seismic imaging of the tectonic zone between the Tibetan Plateau and Ordos Block, central northern China

Ying Li [a], Zhi Chen [a,*], Anhui Sun [a], Zhaofei Liu [b], Antonio Caracausi [c], Giovanni Martinelli [c], Chang Lu [a]

[a] Key Laboratory of Earthquake Prediction (Institute of Earthquake Forecasting, China Earthquake Administration), Beijing 100036, China
[b] School of the Earth and Resources, China University of Geosciences, Beijing 100083, China
[c] INGV-National Institute of Geophysics and Volcanology Dept. of Palermo, Palermo 90146, Italy

ARTICLE INFO

Editor: Christian France-Lanord

Keywords:
Gas geochemistry
Heat flow
Seismic Imaging
Tibetan Plateau
Ordos Block
Convergent boundary

ABSTRACT

The Tibetan Plateau is growing by both vertical uplift and horizontal extension. It is a continuing debate how the Tibetan Plateau interacts with its surrounding plates and blocks. Due to intense tectonic activity, which produced catastrophic earthquakes, the tectonic zone between the northeast margin of the horizontal extending Tibetan Plateau and the stable Ordos Block has garnered considerable interest. This study investigated the spatial distribution of gas geochemical anomalies (e.g., high flux of CO_2 in correspondence of the main faults) at regional scale together with the seismic tomography in correspondence of this tectonic zone with the aim to figure out the domain of convergent boundary between the Ordos block and Tibetan plateau, and trace the tectonic discontinuities which are able to transfer fluids through the crustal layers between the two main geological units. From northwest to southeast, obvious difference of spatial distributions of geochemical and geophysical features in the tectonic zone between the northeast margin of the Tibetan Plateau and the Ordos Block is inferred. The northeast area (Zone A) is dominated by thrust and strike-slip faults with clear velocity boundary underneath, where low crack density (ε), saturation rate (ξ) and Poisson' ratio (σ) in the middle-lower crust coincided with the low values of heat flow and CO_2 emissions, tectonic compression and regional locked-fault can be inducements. The southeast area (Zone C) is dominated by extensional tectonics with roughly *E*-W fast-velocity direction (FVD) of P-wave azimuthal anisotropy, where high permeability and porosity can be deduced from crustal high ε, ξ and relatively high σ anomalies, resulting in high heat flow, CO_2 concentrations and fluxes at the surface, and predominantly crustal-derived gases. The intermediate area (Zone B) also dominated by thrust and strike-slip faults is an extraordinary zone, where intensely locked-fault were clearly revealed, while the predominant anisotropic FVDs in the middle crust changed obviously, more contribution of shallow gas component was detected, and CO_2 flux, heat flow, and regional ε, ξ, and σ in the upper crust were higher, compared with those in Zone A, which indicated the regional crushing fragmentation underneath Zone B. The adopted multidisciplinary approach demonstrated that Zone B is the convergent boundary between the Tibetan Plateau and the Ordos Block.

1. Introduction

The tectonic discontinuities are regions of enhanced porosity and permeability and play a fundamental role in ascending of fluids through the Earth's interior (Ingebritsen and Gleeson, 2017). Therefore, the tectonic zone with strong gas emissions represents effective site for reconstructing regional geodynamic process and monitoring tectonic activity beneath the surface (e.g., Chiarabba and Chiodini, 2013; Caracausi and Sulli, 2019; Randazzo et al., 2021). Furthermore, numerous field investigations had provided several lines of evidence that the fluid geochemistry and gas emissions within a fault zone can provide important constraints for. Revealing hidden faults, tectonic stress accumulation, and seismic activity (Baubron et al., 2002; Ciotoli et al., 1998; Caracausi et al., 2005; Caracausi et al., 2013; Caracausi and Sulli, 2019; Chen et al., 2019; Fu et al., 2017; Vannoli et al., 2021).

Since its onset approximately 55 million years ago, the India-Eurasia collision has created the Tibetan Plateau, with a crustal shortening higher than 2000 km (Molnar et al., 1993; Aitchison et al., 2008). Far-

* Corresponding author.
E-mail address: dugu_830822@163.com (Z. Chen).

https://doi.org/10.1016/j.chemgeo.2023.121386
Received 15 October 2022; Received in revised form 8 February 2023; Accepted 10 February 2023
Available online 15 February 2023

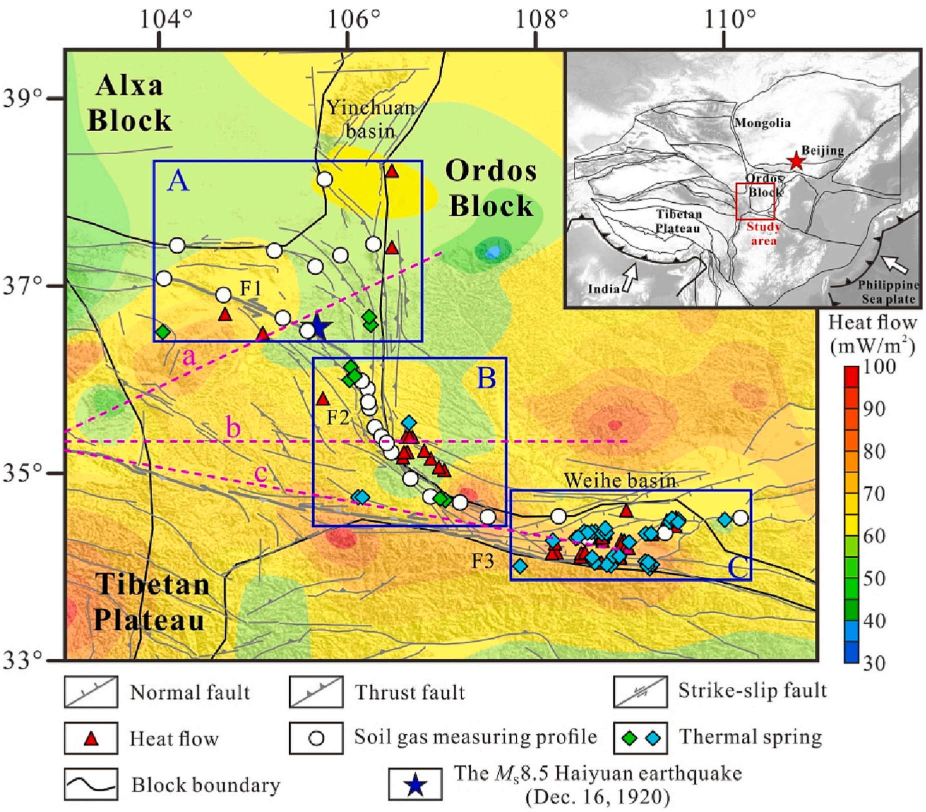

Fig. 1. Regional map of the tectonic contact zone between the Tibetan Plateau and the Ordos Block. Inset shows the location of the study area in China. Purple dashed lines represent the locations of the seismic velocity profiles (a–c), and blue rectangle frames divide the study area into three zones (A–C). The red triangle is heat flow value (http://chfdb.xyz/). White circle is soil gas measuring profile in this study. The green diamond is the thermal spring in this study. The cyan diamond is the thermal spring from previous studies (Wang and Zhang, 1991; Wang, 2008; Xu, 2014; Zhang, 2016; Li et al., 2017; Zhang et al., 2019b). The M_S 8.5 Haiyuan earthquake was from https://data.earthquake.cn. The heat flow map was from Jiang et al. (2019). The block boundary was from Deng et al. (2003). The faults were from Xu et al. (2016) and Rong et al. (2020). F1: the Haiyuan fault zone, F2: the Liupanshan fault zone, F3: the Qinling north fault zone. (For interpretation of the references to colour in this figure legend, the reader is referred to the web version of this article.)

field effects of the continental collision between India and Eurasia continue beyond Tibet into central China, including the Ordos Block. The narrow tectonic contact zone between the Tibetan Plateau and the Ordos Block has drawn significant attention owing to its dramatic tectonic deformation (Tian et al., 2021). Numerous geophysical investigations have been implemented to study the tectonic pattern and evolution of the lower crustal ductile flow beneath the tectonic zone (e.g., Cheng et al., 2016; Klemperer, 2006; Royden et al., 2008; Zhao et al., 2021). Previous regional seismic anisotropy studies had provided important information of this ductile deformation associated with tectonic stress in the crust (e.g., Huang et al., 2017; Li et al., 2011; Sun and Zhao, 2020). Furthermore, regional fluid geochemistry investigation has been performed in the tectonic zone (Li et al., 2017; Sun et al., 2016; Wang and Zhang, 1991; Wang, 2008; Xu, 2014; Zhang, 2016). However,

Table 1
Heat flow values in the study area (http://chfdb.xyz/).

Zone	Number	Longitude (°E)	Latitude (°E)	Heat flow value (mW m^{-2})	Group	Number	Longitude (°E)	Latitude (°E)	Heat flow value (mW m^{-2})
	No.01	106.615	38.245	64.0		No.26	109.233	34.367	96.0
Zone A	No.02	106.674	37.411	54.9		No.27	108.719	34.365	71.9
	No.03	104.700	36.700	73.0		No.28	108.693	34.358	80.2
	No.04	105.100	36.500	58.5		No.29	108.700	34.350	73.0
	No.05	105.740	35.802	64.6		No.30	108.699	34.342	71.2
	No.06	106.650	35.400	69.0		No.31	108.668	34.340	73.9
	No.07	106.667	35.400	69.0		No.32	108.719	34.340	68.5
	No.08	106.662	35.397	59.0		No.33	108.702	34.327	88.6
	No.09	106.913	35.248	50.7		No.34	108.647	34.323	72.0
Zone B	No.10	106.638	35.236	41.6		No.35	108.933	34.300	63.6
	No.11	106.614	35.236	43.3		No.36	108.713	34.297	59.5
	No.12	106.587	35.177	43.3		No.37	108.941	34.293	63.6
	No.13	106.983	35.167	44.5	Zone C	No.38	108.933	34.267	64.0
	No.14	107.106	35.074	80.9		No.39	108.200	34.264	77.0
	No.15	107.100	35.067	66.0		No.40	108.965	34.221	81.7
	No.16	108.961	34.615	67.2		No.41	108.950	34.217	68.0
	No.17	109.491	34.538	62.5		No.42	108.200	34.167	61.0
	No.18	109.393	34.506	64.6		No.43	108.197	34.164	69.0
	No.19	109.483	34.475	66.5		No.44	108.501	34.158	67.4
Zone C	No.20	109.483	34.450	67.0		No.45	108.500	34.158	71.6
	No.21	108.724	34.384	76.5		No.46	108.500	34.150	67.0
	No.22	108.713	34.373	72.0		No.47	108.500	34.151	67.4
	No.23	108.730	34.371	64.1		No.48	108.900	34.117	68.0
	No.24	108.726	34.370	73.4		No.49	108.895	34.114	75.6
	No.25	109.234	34.369	97.7		No.50	108.693	34.064	77.5

Table 2
Statistical parameters of soil gas CO_2 concentration and flux in the study area.

Zone	Number	Profile	Longitude (°E)	Latitude (°E)	Fault	CO_2 concentration (vol%) Mean	Max	Min	CO_2 Flux (g $m^{-2}d^{-1}$) Mean	Max	Min
Zone A	No.01	GGL	104.192	37.426	Guanguanling fault	0.09	0.19	0.06	9.98	10.84	9.13
	No.02	CEG	105.578	36.518	Haiyuan fault	0.67	1.37	0.15	36.21	49.26	24.83
	No.03	WJ	105.316	36.656		0.15	0.30	0.10	14.51	22.78	5.18
	No.04	SQ	104.684	36.898		0.17	0.66	0.07	11.30	30.23	–
	No.05	ST	104.056	37.073		0.15	0.20	0.10	17.30	24.83	10.68
	No.06	STC	106.279	37.441	Luoshan–Niushoushan fault	0.22	0.31	0.12	22.99	23.90	22.08
	No.07	LMG	105.760	38.130		0.09	0.11	0.07	14.51	16.19	12.84
	No.08	SJG	105.661	37.200	Xiangshan–Tianjingshan fault	0.18	0.24	0.13	13.64	15.15	12.14
	No.09	LBG	105.229	37.373		0.19	0.32	0.13	22.99	36.66	9.32
	No.10	WSH	105.930	37.322	Yantongshan fault	0.11	0.13	0.09	18.22	18.67	17.76
Zone B	No.11	BD	106.886	34.756	Guguan–Baoji fault	0.93	1.60	0.63	52.45	103.30	27.03
	No.12	DJ	106.674	34.945	Liupanshan eastern piedmont fault	2.60	5.40	0.10	45.50	63.97	23.43
	No.13	LD	106.469	35.232		1.14	2.65	0.24	15.03	39.27	–
	No.14	XX	106.420	35.327		1.11	2.25	0.37	36.42	57.65	–
	No.15	SLGY	106.365	35.394		1.06	2.13	0.18	38.47	70.41	16.83
	No.16	DZC	106.290	35.498		1.36	2.62	0.44	42.53	54.97	27.64
	No.17	LPC	106.235	35.697		1.46	3.97	0.16	16.70	19.42	13.03
	No.18	YLC	106.222	35.763		1.52	5.98	0.45	17.65	27.28	8.52
	No.19	HJZ	106.213	35.899		0.88	2.91	0.23	37.29	44.70	23.69
	No.20	SYZ	106.151	35.989		0.45	1.28	0.17	53.79	72.21	27.99
	No.21	DY	107.497	34.542	Longxian–Qishan–Mazhao fault	0.54	1.00	0.33	52.76	94.75	–
	No.22	NZ	107.200	34.698		0.90	1.77	0.07	43.47	71.03	30.09
Zone C	No.23	WHC	110.121	34.553	Huashan piedmont fault	0.84	1.60	0.46	110.73	162.26	69.21
	No.24	LT	109.374	34.375	Lishan piedmont fault	0.76	1.76	0.30	254.69	414.21	166.91
	No.25	XP	108.553	34.312	Weihe fault	1.30	3.32	0.55	172.14	202.93	128.60
	No.26	QX	108.248	34.550	Yidian–Qianxian–Meiyuan fault	0.47	0.89	0.20	90.36	124.19	48.87

"-" means no data.

no coupled investigation has so far been carried out to reveal the possible links between gas geochemical characteristics and geophysical parameters of the tectonic zone, which is an urgent question for understanding the tectonic development of the Tibetan plateau surrounding and the seismicity in the tectonic zone (Ordos block vs. Tibetan Plateau).

In this study, we investigated the spatial distribution of the fluid geochemical feature, heat flow and the coupled seismic anisotropic image in the tectonic zone between the northeast margin of the Tibetan Plateau and the Ordos Block. Based on the results, we identified the convergent boundary between the Tibetan Plateau and the Ordos Block and its tectonic feature.

2. Geological setting

2.1. Tectonics

Since ~55 Ma, the convergence of the Indian and Eurasian plates has resulted in shortening and deformation of the latter, with the compressive stress transmitted to the northeast margin of the Tibetan Plateau and blocked by the Ordos Block (Burchfiel et al., 1991; Yin and Harrison, 2000). The interaction between the Tibetan Plateau and the Ordos Block controls the seismic activity at regional scale along deep-seated faults (e.g., Yin et al., 2002; Kusky et al., 2016; Lei and Zhao, 2016).

Based on the tectonic settings, and regional stress states, the study area is divided into three zones (A–C) (Fig. 1; Liu et al., 2008; Wang et al., 2011; Zhang et al., 2019a; Rong et al., 2020). Zone A is an arc tectonic belt located between the Tibetan Plateau, Alxa Block and Ordos Block (Fig. S1). Subjected to the continued tectonic compression, several thrust arcuate faults were formed which converge southward and diverge northward (Burchfiel et al., 1991; Sun et al., 2016; Zhan et al., 2017). Zone B marks the convergent boundary between the Tibetan Plateau and the Ordos Block (Fig. S2). It covers the Liupanshan fault zone, a narrow zone with clustered strike-slip faults in the compressional tectonic stress environment (Chai et al., 2003; Cheng et al., 2016; Tian et al., 2021). Zone C overlays the Weihe basin (Fig. S3), an extensional rift system including several normal faults (Wang, 2008; Zhang et al., 2019a; Zhang et al., 2019b).

According to available catalogues, there have been 49 mainshocks of magnitude 6 or above within this tectonic zone since 1970 (Chai et al., 2003). The heat flow pattern of the tectonic zone is heterogenous, with values ranging from 41.6 to 97.7 mW m^{-2} (Table 1), Zone B shows higher values than A and C (Fig. 1), which is mostly a result of Meso-Cenozoic tectonic activity (Jiang et al., 2019).

3. Methodology

3.1. Gas measurements and sampling

The concentrations and fluxes of CO_2 in soil gas were measured in the field along 26 profiles approximately perpendicular to the strike direction of the faults (Fig. 1, Table 2). Sampling sites along the profiles were at intervals of 5–40 m (5 m near fault scarps and lengthening gradually to the ends of the survey line away from fault scarps). Flux measurements were performed at sampling sites within fracture zones; the total number of flux measurements per profile was 2–4. In total, we optimized 508 concentration and 92 flux measurements for both CO_2 soil gas.

CO_2 concentration was performed by inserting a stainless-steel sampling tube with a diameter of 3 cm into the ground to a depth of 80 cm; reaching this depth is important for minimizing meteorological effects (Hou et al., 1994). The sampling tube was connected to the CO_2 monitor using a rubber tube. The CO_2 concentration value was obtained when the concentration value on the LCD screen became invariable for about 20 s. CO_2 fluxes were measured using the static closed chamber method; the instrument included an inverted circular accumulation hemispherical chamber with a volume of 1.68×10^{-2} m^3 and a radius of 0.2 m. The CO_2 concentrations and fluxes were measured by a portable infrared CO_2 monitor (GXH-3010-E for CO_2 concentration) with a detection limit of 0.01 vol%, respectively. An inlet filter and molecular sieve were used to protect the detector from dust and soil moisture.

Bubbling spring gas samples were collected in cylindroid glass bottles (500-ml volume, made of soda-lime glass with a 0.5-cm thickness) to measure the helium isotopic ratios ($^3He/^4He$, reported as R/Ra where R

Table 3
Analysis of gas from springs in the study area.

Zone	Spring	Longitude (°E)	Latitude (°E)	$^3He/^4He$	R/Ra	Rc/Ra	$^4He/^{20}Ne$	CO_2 concentration (vol%)	$\delta^{13}C_{CO2}$ (‰)	References
Zone A	No.01	103.928	36.455	1.10×10^{-8}	0.01	0.01	1048	1.04	–	This study
	No.02	106.252	36.587	1.03×10^{-7}	0.07	0.07	841	6.32	−10.70	
	No.03	106.253	36.587	7.21×10^{-8}	0.05	0.05	1611	9.89	–	
Zone B	No.04	106.040	36.131	9.89×10^{-8}	0.07	0.05	15	–	−16.79	
	No.05	106.082	36.019	3.12×10^{-8}	0.02	0.02	158	0.08	−15.13	
	No.06	106.083	36.018	1.70×10^{-8}	0.01	0.01	313	0.14	–	
	No.07	106.661	35.543	5.80×10^{-7}	0.40	–	–	–	–	Wang, 2008
	No.08	106.121	34.752	6.08×10^{-8}	0.04	–	–	–	–	
	No.09	106.133	34.749	7.31×10^{-8}	0.05	–	–	–	–	Wang and Zhang, 1991
	No.10	106.991	34.737	7.33×10^{-7}	0.52	–	–	1.02	–	This study
	No.11	106.992	34.736	1.41×10^{-8}	0.01	–	11	0.62	−17.97	
Zone C	No.12	107.842	34.019	1.34×10^{-7}	0.10	–	–	–	–	Wang, 2008
	No.13	108.182	34.301	5.04×10^{-8}	0.04	0.04	6000	3.77	−8.06	Zhang et al., 2019b
	No.14	108.420	34.330	5.32×10^{-8}	0.04	0.04	2675	2.66	−9.16	
	No.15	108.451	34.336	4.62×10^{-8}	0.03	0.03	5227	4.79	−10.50	
	No.16	108.527	34.382	9.54×10^{-8}	0.07	0.07	2114	–	–	Xu, 2014
	No.17	108.552	34.352	8.68×10^{-8}	0.06	0.06	1110	–	–	
	No.18	108.581	34.356	9.98×10^{-8}	0.07	0.07	1590	–	–	
	No.19	108.604	34.112	4.70×10^{-8}	0.03	0.03	357	–	–	
	No.20	108.635	34.055	6.05×10^{-8}	0.05	0.04	226	–	–	
	No.21	108.641	34.343	8.99×10^{-8}	0.06	–	–	–	–	Wang, 2008
	No.22	108.703	34.371	9.24×10^{-8}	0.07	0.07	9329	9.36	−10.42	Zhang et al., 2019b
	No.23	108.731	34.436	9.94×10^{-8}	0.07	0.07	5526	2.09	−8.98	
	No.24	108.737	34.383	6.72×10^{-8}	0.05	0.05	5912	31.69	−5.77	
	No.25	108.759	34.038	9.43×10^{-8}	0.07	0.07	139	–	–	Li et al., 2017
	No.26	108.779	34.035	1.32×10^{-7}	0.09	0.09	142	–	–	
	No.27	108.829	34.125	5.02×10^{-8}	0.04	0.04	1011	–	–	Xu, 2014
	No.28	108.895	34.125	5.07×10^{-8}	0.04	0.04	1010	–	–	
	No.29	108.998	34.271	5.56×10^{-8}	0.04	0.04	163	–	–	
	No.30	109.174	34.363	3.86×10^{-7}	0.28	–	–	–	–	Wang, 2008
	No.31	109.198	34.063	1.26×10^{-7}	0.09	0.09	132	–	–	Xu, 2014
	No.32	109.198	34.063	1.24×10^{-7}	0.09	–	–	–	–	Wang, 2008
	No.33	109.214	34.016	1.26×10^{-7}	0.09	0.09	132	–	–	Zhang, 2016
	No.34	109.218	34.020	7.80×10^{-7}	0.56	0.56	1500	–	–	Xu, 2014
	No.35	109.218	34.016	1.11×10^{-7}	0.08	0.08	146	–	–	Zhang, 2016
	No.36	109.227	34.367	4.20×10^{-8}	0.03	0.21	439	–	–	Xu, 2014
	No.37	109.424	34.500	9.80×10^{-8}	0.07	0.07	8319	22.24	−5.47	Zhang et al., 2019b
	No.38	109.441	34.528	1.11×10^{-7}	0.08	0.08	5595	13.56	−7.49	
	No.39	109.473	34.500	1.49×10^{-7}	0.11	0.11	1987	–	–	Xu, 2014
	No.40	109.490	34.512	1.27×10^{-7}	0.09	0.09	3212	–	–	
	No.41	109.502	34.498	9.80×10^{-8}	0.07	0.07	5111	7.42	−8.23	Zhang et al., 2019b
	No.42	110.092	34.542	1.00×10^{-7}	0.07	0.07	2562	–	–	Xu, 2014

"-" means no data.

is the $^3He/^4He$ in the gas sample and Ra is the He isotopic signature in atmosphere), the $^4He/^{20}Ne$ ratios and the $\delta^{13}C_{CO2}$ values in free gases, the helium diffusion in this type of glass bottle had been proved to be negligible (Chen et al., 2019). In this study, 8 springs were sampled and 8 bottles of spring gas were collected from each sampling spring site in September 2018; other data were indexed from published articles (Table 3). The methods for gas sampling are reported in (Zhou et al., 2015).

3.2. Laboratory analysis

The $^3He/^4He$ (reported as R/Ra, Ra = 1.4×10^{-6}, Sano and Wakita, 1985) and $^4He/^{20}Ne$ were determined using a MM5400 mass spectrometer, with uncertainties of ±3‰, in the Analytical Laboratory of the Beijing Research Institute of Uranium Geology. The minimum heat blanks of the MM5400 mass spectrometer are 1.10×10^{-14} (mol) for ^4He and 1.82×10^{-14} (mol) for ^{20}Ne, respectively (Ye et al., 2007). The $\delta^{13}C_{CO2}$ values of the gas samples were analyzed with uncertainties of ±0.3 ‰ at the Key Laboratory of Petroleum Resources Research, Institute of Geology and Geophysics, Chinese Academy of Science. A GC-IRMS analytical system gas chromatograph (Agilent 6890)-stable isotope ratio mass spectrometer (Thermo-Fisher Scientific Delta Plus XP) was used for carbon isotopic ratio analysis. The $\delta^{13}C_{CO2}$ values were reported relative to PDB (Ye et al., 2001).

3.3. Crack density and saturation rate by seismic tomography

Poisson's ratio (σ), equivalently V_P/V_S, is used to determine the composition of the crust (e.g., Christensen and Mooney, 1995; Christensen, 1996). Partially molten materials or fluids reduce V_S significantly, and cause high σ anomalies. Additionally, cracks and fluids in the crust could also contribute to changes of the Poisson's ratio (O'Connell and Budiansky, 1974). The crack theory (O'Connell and Budiansky, 1974) links the changes in Poisson's ratio (σ) to the crack density (ε) and saturation rate (ξ) parameters of rocks, allowing for the estimation of crack density and saturation rate in stressed rocks through seismic velocity data (Zhao and Mizuno, 1999).

Crack density (ε) is defined as (O'Connell and Budiansky, 1974):

$$\varepsilon = N\langle a^3 \rangle \tag{1}$$

where a is the radius for circular cracks and N the number of cracks per unit volume, and suppose that dry cracks per unit volume are N_1, and then saturated cracks $N_2 = N - N_1$, hence the saturated rate (ξ) is defined as:

$$\xi = N_2/N \tag{2}$$

As Sun et al. (2021) mentioned, we firstly inverted a high-resolution crustal P and S wave velocity structure by using arrival-time data recorded at 872 seismic stations in NE Tibet, including 154 regional seismic stations of the China Seismic Network (CSN), 718 temporary

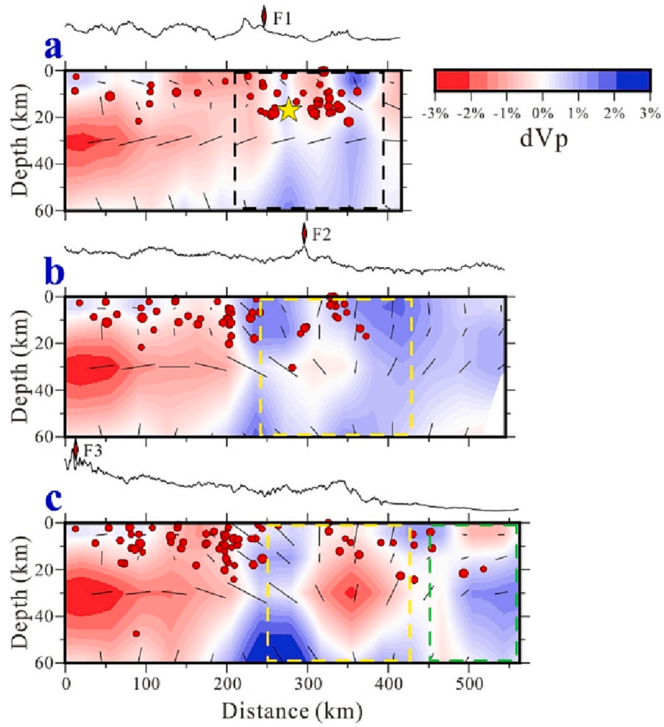

Fig. 2. Cross-sectional seismic anisotropy images of P-wave velocity variation (dV_P) along the 3 profiles shown in Fig. 1. Colour scales are shown in the top-right. Black, yellow, and green dashed rectangles denote Zones A, B, and C, respectively. Red dots denote epicenters of earthquakes (M > 3.0) within ~30 km of each profile from 1970 to 2017 (https://data.earthquake.cn). The black, short and solid line denotes the FVD of P-wave azimuthal anisotropy. The yellow star denotes the epicenter of the 1920 Haiyuan 8.5 earthquake (https://data.earthquake.cn). The surface topography is shown above each cross-section. The red diamonds denotes the position of large active fault zones, F1: the Haiyuan fault zone, F2: the Liupanshan fault zone, F3: the Qinling north fault zone. (For interpretation of the references to colour in this figure legend, the reader is referred to the web version of this article.)

stations of the ChinArray project (2013.10–2016.04) and the Seismic Array Cross Hai-Yuan Fault project (2012–2013). Then Poisson's ratio (σ) is obtained with the relationship (Zhao et al., 1996):

$$\frac{V_P}{V_S} = \sqrt{\frac{2(1-\sigma)}{(1-2\sigma)}} \tag{3}$$

Finally, we estimate ε and ξ by following equations of O'Connell and Budiansky (1974):

$$\varepsilon = \frac{45}{16}\left(\frac{\sigma-\overline{\sigma}}{\sigma-\overline{\sigma}^2}\right)\frac{2-\overline{\sigma}}{(1-\xi)(1+3\sigma)(2-\overline{\sigma})-2(1-2\sigma)} \tag{4}$$

$$\xi = 1-\frac{2(1-2\overline{\sigma})}{(2-\overline{\sigma})(1+3\overline{\sigma})} \tag{5}$$

where σ and $\overline{\sigma}$ are Poisson's ratios for uncracked and cracked volumes, respectively. Magnetotelluric surveys detected low resistivity (i.e., high electric conductivity) phenomenon around our study area (Zhan et al., 2017; Zhao et al., 2005), which has a close relationship with a combination of partial melts and salt aqueous fluids (Wei et al., 2001). The spatial and temporal change of fluids in the active fault zones will affect pore pressure and permeability, characteristic parameters of fractured rocks. Thus, σ variations with estimated ε and ξ in high-resolution can help to detect the existence and migration of fluids in the relative homogenous crust of small-scale.

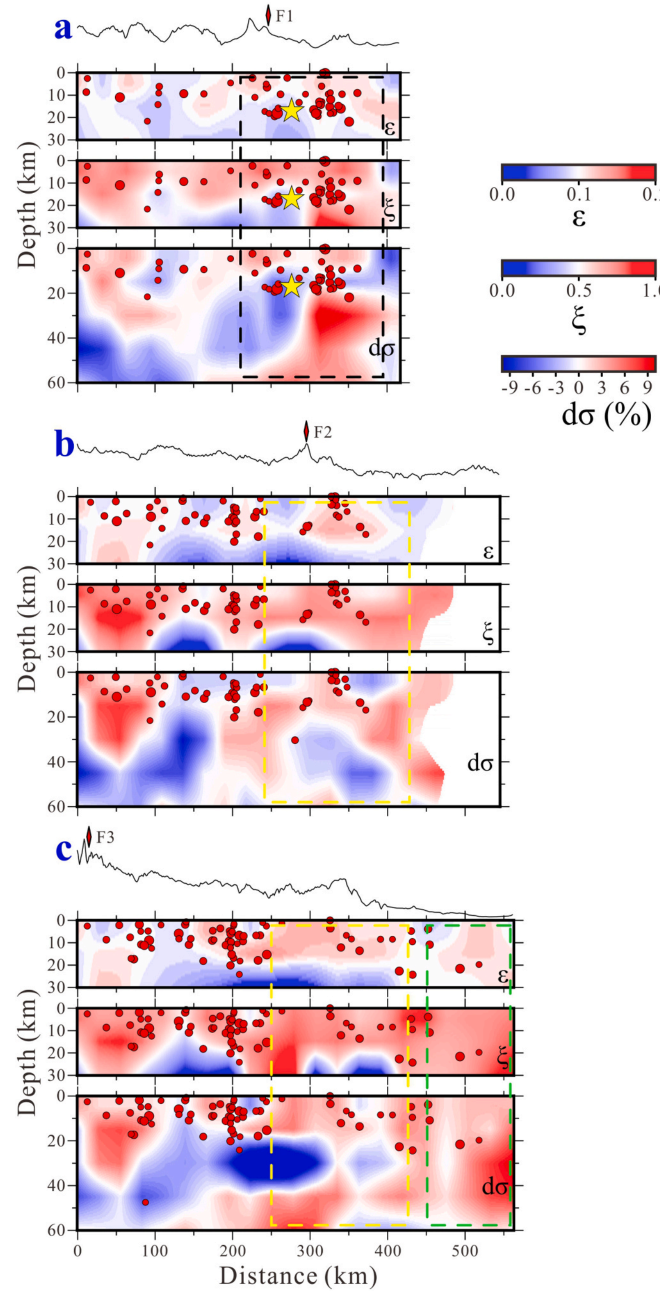

Fig. 3. Cross-sectional seismic images of crack density (ε), saturation rate (ξ), and Poisson's ratio (σ) along the 3 profiles shown in Fig. 1. Colour scales are shown in the top-right. Black, yellow, and green dashed rectangles denote Zones A, B, and C, respectively. Red dots denote epicenters of earthquakes (M > 3.0) within ~30 km of each profile from 1970 to 2017 (https://data.earthquake.cn). The purple dotted line denotes the deduced convergent boundary. The yellow star denotes the epicenter of the 1920 Haiyuan 8.5 earthquake (https://data.earthquake.cn). The surface topography is shown above each cross-section. The red diamonds denotes the position of large active fault zones, F1: the Haiyuan fault zone, F2: the Liupanshan fault zone, F3: the Qinling north fault zone. (For interpretation of the references to colour in this figure legend, the reader is referred to the web version of this article.)

4. Results

4.1. Geochemistry of fluids

The concentrations and fluxes of CO_2 in soil gas in correspondence of the trace at the surface of the main active fault zones in the study area

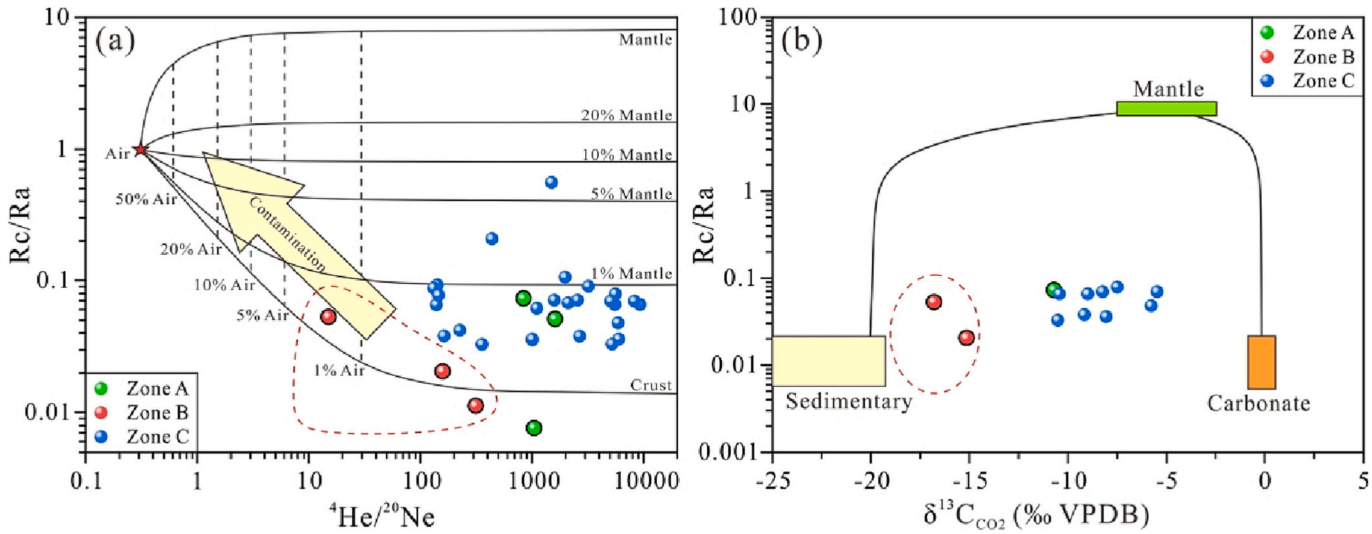

Fig. 4. Correlation among isotope values of spring gas samples in the study area. (a) $^3He/^4He$ (R/Ra) vs. $^4He/^{20}Ne$, $(R/Ra)_{Air} = 1.0$ Ra, $(^4He/^{20}Ne)_{Air} = 0.318$ (Sano and Wakita, 1985); $(R/Ra)_{Mantle} = 8.0$ Ra, $(^4He/^{20}Ne)_{Mantle} = 1000$ (Graham, 2002); $(R/Ra)_{Crust} = 0.02$ Ra, $(^4He/^{20}Ne)_{Crust} = 1000$ (Andrews, 1985); (b) $He/^4He$ (R/Ra) vs. $\delta^{13}C_{CO2}$ (modified from Etiope et al., 2011). The circle with black line represents the data of this study. The circle without black line represent data from previous studies (Wang and Zhang, 1991; Wang, 2008; Xu, 2014; Zhang, 2016; Li et al., 2017; Zhang et al., 2019b).

are listed in Table 2. The minimum and maximum measured soil gas CO_2 concentrations ranged from 0.06 to 0.63% and from 0.11 to 5.98%, respectively; the mean concentrations ranged from 0.09 to 2.60%. All of these values are higher than the CO_2 concentrations in atmosphere (418.19 ppm; https://gml.noaa.gov/ccgg/trends/). The minimum and maximum fluxes of soil gas CO_2 varied from 5.18 to 166.91 g m^{-2} d^{-1} and from 10.84 to 414.21 g m^{-2} d^{-1}, respectively; the mean fluxes ranged from 9.98 to 254.69 g m^{-2} d^{-1}.

The $^3He/^4He$ and $^4He/^{20}Ne$ of the 42 spring gas samples ranged from 1.10×10^{-8} to 7.80×10^{-7} and from 11 to 9329, respectively, and they are compatible to the literature data in the study region. The $\delta^{13}C_{CO2}$ values of the spring gas samples were in the range of $-17.97 \sim -5.47$‰, with the CO_2 concentrations in the range of 0.08–31.69% (Table 2).

4.2. Seismic anisotropy tomography

Vp changed abruptly beneath the Haiyuan fault in Zone A, similar as those near the Liupanshan fault in Zone B, where the predominant FVDs underneath generally became strike-parallel (Fig. 2). In addition, local low-velocity anomalies exhibited in the upper crust under the Zones A and C, while in the upper-middle crust under Zone B. In addition, the predominant FVDs underneath also generally became strike-parallel under Zone B (Figs. 2b and c).

Previous studies have shown that the crack density in the middle-upper crust is small ($\varepsilon \le 0.2$; Sun et al., 2021) and that seismic anisotropy is strong in the deep crust (Sun and Zhao, 2020) under NE Tibet. Hence, following the instructions of O'Connell and Budiansky (1974), we estimated three-dimensional (3-D) distributions of crack density (ε) and saturation rate (ξ) for the crust of the study area. Strong structure heterogeneities were presented in the crust beneath the study area (Fig. 3). In addition, an anomalous layer of low-ε, low-ξ, and relatively low-σ were exhibited in the middle-lower crust beneath Zones A and B (Fig. 3a and b). In contrast, high-ε, high-ξ, and relatively high-σ anomalies were revealed in the crust beneath Zone C (Fig. 3c).

5. Discussion

The correlations of $^3He/^4He$ (R/Ra) vs. $^4He/^{20}Ne$ and $^3He/^4He$ (R/Ra) vs. $\delta^{13}C_{CO2}$ of gases sampled from springs within the fault zones provide evidence for a dominant crustal component for the gases degassing in the three Zones A, B and C between the northeast margin of the Tibetan Plateau and the Ordos Block (Fig. 4). Active faults are preferred pathways that contribute to gas migration (e.g., Caracausi et al., 2005, 2013; Caracausi and Sulli, 2019; Buttitta et al., 2020; Chen et al., 2019; Tamburello et al., 2018). It suggests 1) all the faults in the three Zones A, B and C between the northeast margin of the Tibetan Plateau and the Ordos Block have not extended to the mantle, or were impervious within the mantle, 2) the release of crustal ^4He along the fault zone because of variation of the stress field (e.g., Caracausi and Paternoster, 2015; Buttitta et al., 2020) and 3) the long residence time within the crust for the gases. However, the points for the gas sampled from springs within Zone B shift toward the Air end-member and Sedimentary end-member in the graphs of $^3He/^4He$ (R/Ra) vs. $^4He/^{20}Ne$ and $^3He/^4He$ (R/Ra) vs. $\delta^{13}C_{CO2}$, respectively (Fig. 4), which suggests more contribution of shallow component (air contamination or sedimentary gas) for the gases along the faults within Zone B than those in Zones A and C.

In addition, the maximum values of soil gas CO_2 concentration and flux were observed in correspondence of the faults in Zone B and Zone C, respectively (Table 2). The mean CO_2 concentration (1.16%) of soil gas emission along the deduced convergent boundary within Zone B was 5.75 and 1.38 times as those of Zones A and C (0.20% and 0.84%, respectively), and the mean CO_2 flux (37.67 g $m^{-2}d^{-1}$) was 2.07 and 0.24 times as those of Zones A and C (18.17 and 156.98 g $m^{-2}d^{-1}$, respectively) (Fig. 5a and b). In fact, extensional tectonics could facilitate fracture development, causing a stronger degassing at regional scale in the normal fault zones than the thrust and strike-slip faults (Tamburello et al., 2018). Therefore, it is reasonable that the CO_2 emission was stronger in Zone C where regional extension and normal faults dominate, than those in Zones A and B where intense compression and strike-slip dominate the tectonic at regional scale (Figs. 1 and 5). However, unexpectedly, in Zone B where most of the faults were intensely locked (Fig. 5c), the maximum values of CO_2 concentration were presented (Fig. 5a), and the mean CO_2 flux was also more than two times as that in Zone A where limited fault section was locked (Fig. 5c, Table 2). In addition, higher heat-flow values were presented in Zone B (41.6–80.9 mW/m^2) and C (59.5–97.7 mW/m^2) than that in Zone A (54.9–73.0 mW/m^2) (Fig. 5d). Therefore, some special spatial variability in the regional geodynamic framework for the tectonic zone between the Tibetan Plateau and Ordos Block was considered.

Thus, here we explored the deep crustal structure by means of seismological methods that consider seismic later phases (Sun et al., 2019,

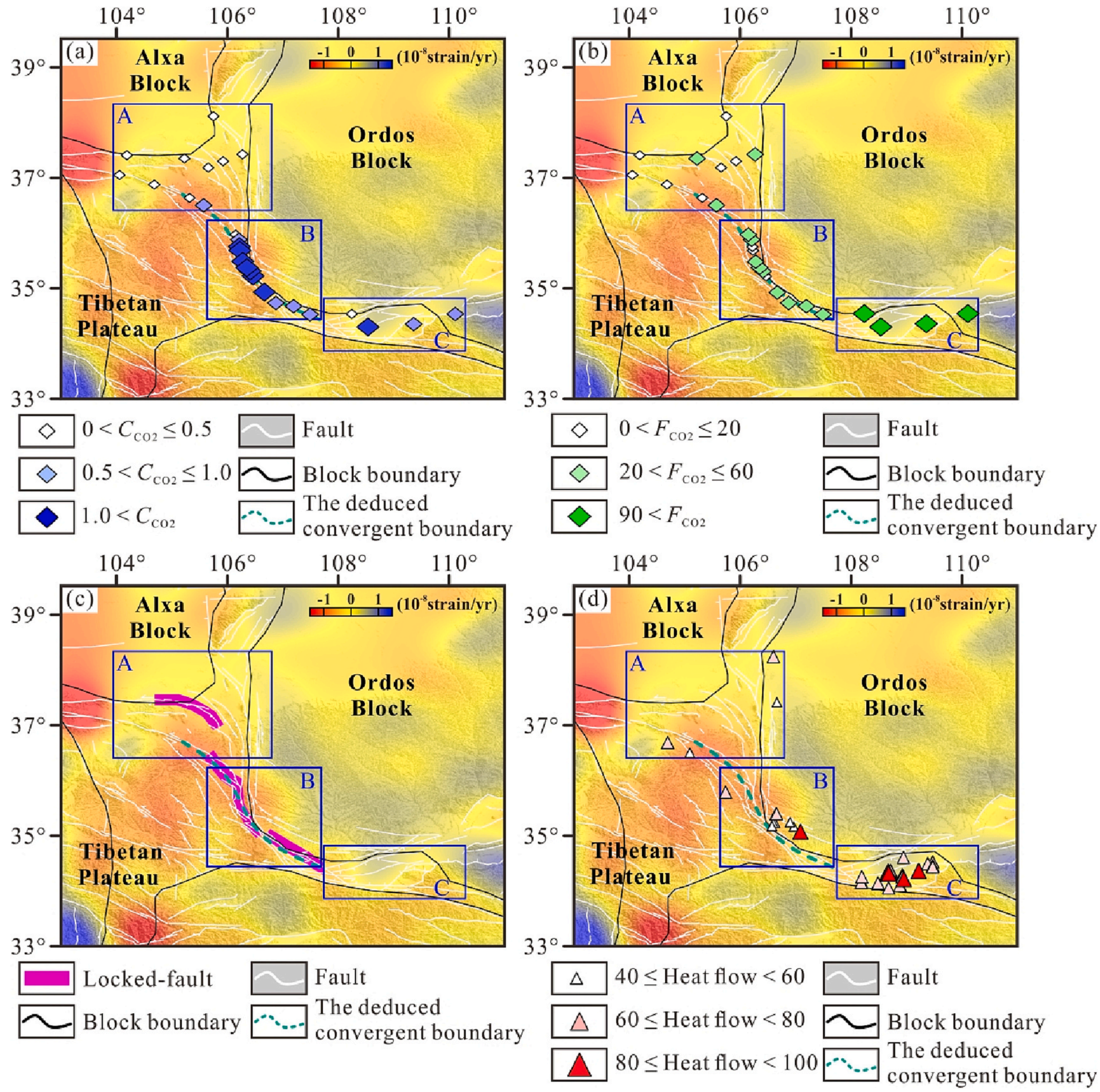

Fig. 5. Spatial distributions of the concentrations and fluxes of soil gas CO_2 and heat flow in the study area. (a) CO_2 concentration (C_{CO2}, vol%); (b) CO_2 flux (F_{CO2}, g m^{-2} d^{-1}); (c) Location of locked-fault (Shao et al., 2022). The background is distribution of dilatation stain rate (Li et al., 2018); (d) Heat flow (in mW m^{-2}; http://chfdb.xyz/).

2021; Zhao et al., 2005). Based on P-Wave azimuthal anisotropic results (Sun and Zhao, 2020), obvious longitudinal boundary between low-velocity zone and high-velocity zone under NE Tibet was delineated, which has been confined by the Haiyuan fault in Zone A and the Liupanshan fault in Zone B (Fig. 2).

In Zone C, a rift basin dominated by extensional tectonics, high permeability, porosity, and the upwelling of deep-derived gas can be deduced from heterogeneous and high-ε, high-ξ, and relatively high-σ in the crust (Fig. 3), resulting in high heat flow, CO_2 concentrations and fluxes (Fig. 5a, b and d), and predominantly crustal-derived gases (Fig. 4). Homogenous ε, ξ and σ in the crust and low ε, ξ, and σ in the middle-lower crust were presented in both Zones B and A (Fig. 3), dominated by thrust and strike-slip faults (Fig. 1). It could indicate that both Zones B and A have undergone substantial tectonic compression, as presented by the dilatation stain rate (Fig. 5), and pre-existing fractures could be partially closed and permeability of the strata has decreased (Fig. 3). Thus, the uprising of gases and heat from depth is likely obstructed or takes a longer time in Zones B and A. Hence, in Zone A where limited fault section was locked, although predominantly crustal-derived gases was observed from the springs (Fig. 4), coupled distribution of weak gas emission and low heat flow was pronounced (Fig. 5). In addition, compared with Zone A, regional higher ε, ξ, and σ in the upper crust were detected in Zone B where most of the faults were once intensely locked, and the anisotropic FVDs changed obviously from W-E toward N-S under Zone B (Fig. 2). Therefore, further regional fragmentation in the shallow sedimentary formation under the intense compression can be inferred along the deduced convergent boundary within Zone B (Fig. 6), which was responsible for the obvious high CO_2 concentration of the soil gas from the fault (Fig. 5a), slightly high CO_2 flux and heat flow (Fig. 5b and d), while more contribution of shallow component for the gases degassing from the faults within Zone B (Fig. 5).

Based on the above discussion, we inferred that the Tibetan Plateau has dominantly bordered on the rigid Ordos block, during its north-eastward movement due to the remote action of the India-Eurasia collision, and the convergent boundary should be primarily within Zone B (Fig. 6), which acts as a crustal-wedge of the Ordos crust inserted into the Longxi crust (Tian et al., 2021) as a high-velocity zone (Sun et al., 2019). As the crust shortening and tectonic compression continuously increasing, stress accumulation can be performing in both Zone B and A (Fig. 6), and Zone B should be the focal region, which have undergone more intense deformation than Zone A and been once intensely locked (Fig. 5c). Nowadays, subjected to the further tectonic collision

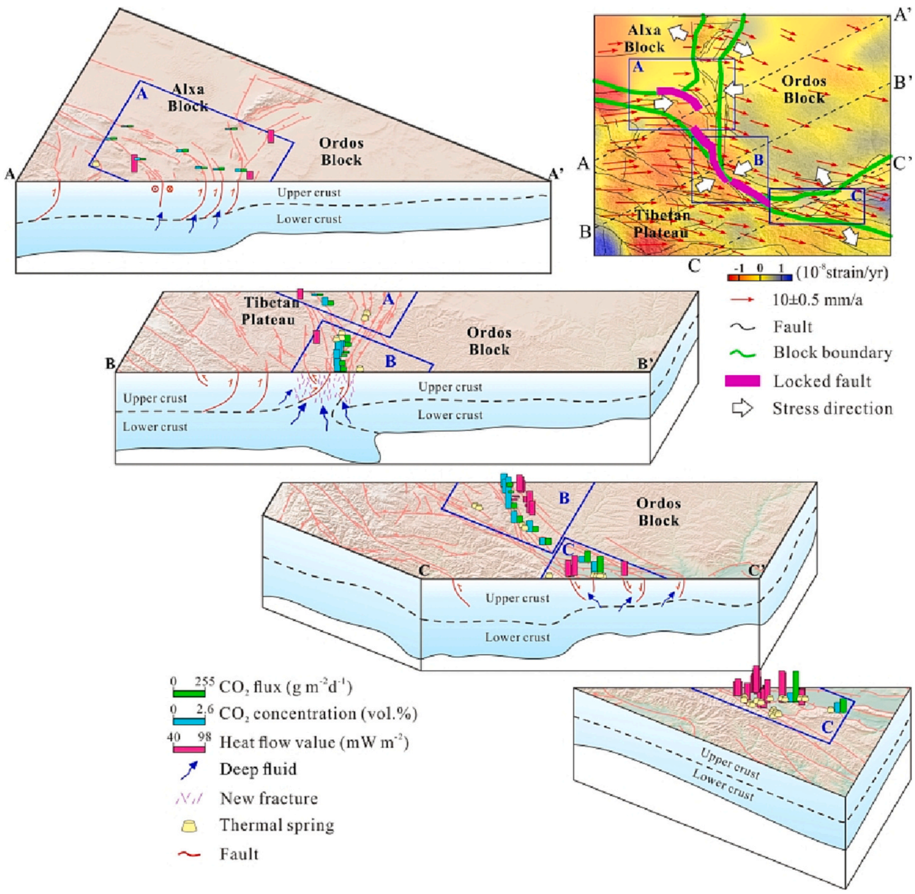

Fig. 6. Schematic model showing 3D sketches of tectonic features of the Tibetan Plateau-Ordos Block contact zone.

and stress-concentration within the convergent boundary as seismic anisotropy suggested (Fig. 2b), primary regional fragmentation have occurred in the shallow sedimentary formation along the deduced convergent boundary within Zone B, which could result in the regional higher ε, ξ, and σ in the upper crust, and facilitate the circulation of gases through the new developing failure. Thus, obvious higher CO_2 concentration of the soil gas from the fault (Fig. 5a), slightly higher CO_2 flux and heat flow (Fig. 5b and c), while more contribution of shallow component for the gases degassing from the faults were observed within Zone B than those in Zone A. However, extensional tectonics have been verified to facilitate fracture development, causing a stronger degassing in the normal fault Zones than the thrust and strike-slip faults (Tamburello et al., 2018). Therefore, it is expected that high-ε, high-ξ, and relatively high-σ in the crust, high heat flow, CO_2 concentrations and fluxes, and predominantly crustal-derived gases were detected in Zone C, a rift basin dominated by extensional tectonics.

6. Conclusions

In this study, we analyzed the fluid geochemical feature, heat flow and geophysical imaging in the tectonic zone between the Tibetan Plateau and the Ordos Block, central northern China. Based on our results, three main conclusions can be summarized as follows:

(1) Active faults are pathways along which deep fluids and heats can migrate to the Earth's surface. However, in the tectonic zone between the Tibetan Plateau and the Ordos Block, there was a clear spatial heterogeneity in fluid geochemical feature, heat flow emissions, and geophysical imaging.

(2) In Zone C dominated by extensional tectonics, unexcepted homogeneous high-ε, high-ξ, and relatively high-σ in the crust, high heat flow, CO_2 concentrations and fluxes, and predominantly crustal-derived gases were detected there. In Zone A dominated by thrust and strike-slip faults, where limited fault section was locked, low ε, ξ, and σ in the middle-lower crust were found together with weak gas emission and low heat flow. Zone B is also dominated by thrust and strike-slip faults, where most of the faults were once intensely locked, compared with Zone A, higher CO_2 flux, heat flow, and regional higher ε, ξ, and σ in the upper crust were presented, and the CO_2 concentration there was even higher than that in Zone C, although more contribution of shallow component was detected there.

(3) Zone B is the convergent boundary between the Tibetan Plateau and the Ordos Block. The geological formations below Zone B can have undergone more intense deformation than those of Zone A, subjected to the further tectonic collision and stress-concentration within the convergent boundary, primary regional fragmentation can have occurred in the shallow sedimentary formation.

CRediT authorship contribution statement

Ying Li: Conceptualization, Funding acquisition, Investigation, Writing – review & editing. **Zhi Chen:** Writing – original draft, Investigation, Methodology. **Anhui Sun:** Writing – review & editing, Investigation, Visualization. **Zhaofei Liu:** Formal analysis, Investigation, Methodology, Visualization, Software. **Antonio Caracausi:** Conceptualization, Investigation, Writing – review & editing. **Giovanni Martinelli:** Investigation, Methodology, Writing – review & editing. **Chang Lu:** Investigation.

Declaration of Competing Interest

(1) All authors disclosed no relevant relationships.

(2) The authors declared no potential conflict of interest with respect to the research, author- ship, and/or publication of this article.

Data availability

Data will be made available on request.

Acknowledgments

This work was supported by the National Key Research and Development Program of China [Grant number 2019YFC1509203] and National Natural Science Foundation of China [Grant number 41402298, 42073063, and 41974050]. This work is a contribution to IGCP Project 724. Research data associated with this article had been uploaded to Mendeley Data (https://DOI:10.17632/5bnvwxmtv8.1). The dataset was in moderation, which can be accessed from an open access repository at Mendeley Data when it is accepted.

Appendix A. Supplementary data

Supplementary data to this article can be found online at https://doi.org/10.1016/j.chemgeo.2023.121386.

References

Aitchison, J.C., Ali, J.R., Davis, A.M., 2008. When and where did India and Asia collide ? Geol. Bull. China. 27 (9), 1351–1370.

Andrews, J.N., 1985. The isotopic composition of radiogenic helium and its use to study groundwater movement in confined aquifers. Chem. Geol. 49 (1–3), 339–351. https://doi.org/10.1016/0009-2541(85)90166-4.

Baubron, J.C., Rigo, A., Toutain, J.P., 2002. Soil gas profiles as a tool to characterize active tectonic areas: the Jaut Pass example (Pyrenees, France). Earth Planet. Sci. Lett. 196, 69–81. https://doi.org/10.1016/S0012-821X(01)00596-9.

Burchfiel, B.C., Zhang, P.Z., Wang, Y.P., Zhang, W.Q., Song, F.M., Deng, Q.D., Molnar, P., Royden, L., 1991. Geology of the Haiyuan Fault Zone, Ningxia-Hui Autonomous Region, China, and its relation to the evolution of the Northeastern margin of the Tibetan Plateau. Tectonics. 10 (6), 1091–1110. https://doi.org/10.1029/90tc02685.

Buttitta, D., Caracausi, A., Chiaraluce, L., Favara, R., Morticelli, M.G., Sulli, A., 2020. Continental degassing of helium in an active tectonic setting (northern Italy): the role of seismicity. Sci. Rep. 10, 162. https://doi.org/10.1038/s41598-019-55678-7.

Caracausi, A., Paternoster, M., 2015. Radiogenic helium degassing and rock fracturing: a case study of the southern Apennines active tectonic region. *J. Geophys. Res.-Solid.* Earth. 120 (4), 2200–2211. https://doi.org/10.1002/2014jb011462.

Caracausi, A., Sulli, A., 2019. Outgassing of mantle volatiles in compressional tectonic regime away from volcanism: the role of continental delamination. Geochem. Geophys. Geosyst. 20, 2007–2020. https://doi.org/10.1029/2018GC008046.

Caracausi, A., Favara, R., Italiano, F., Nuccio, P.M., Paonita, A., Rizzo, A., 2005. Active geodynamics of the central mediterranean sea: tensional tectonic evidences in western sicily from mantle-derived Helium. Geophys. Res. Lett. 32, L04312. https://doi.org/10.1029/2004GL021608.

Caracausi, A., Martelli, M., Nuccio, M., Paternoster, M., 2013. Active degassing of mantle-derived fluids: a geochemical study along the Vulture Line, Southern Appennines (Italy). J. Volcanol. Geotherm. Res. 253, 65–74. https://doi.org/10.1016/j.jvolgeores.2012.12.005.

Chai, C.Z., Ma, H.Q., Jin, C.H., 2003. Features of moderate-strong earthquake activity and anomalous features before earthquakes in Qilian Mt.–Liupan Mt. earthquake belt. Northwestern Seismological J. 25, 354–358 (in Chinese with an English abstract). https://doi.org/10.3969/j.issn.1000-0844.2003.04.012.

Chen, Z., Li, Y., Liu, Z.F., Zheng, G.D., Xu, W., Yan, W., Yi, L., 2019. CH_4 and CO_2 emissions from mud volcanoes on the southern margin of the Junggar Basin, NW China: Origin, output, and relation to regional tectonics. J. Geophys. Res.-Solid Earth 124, 1–15. https://doi.org/10.1029/2018jb016822.

Cheng, B., Zhao, D., Cheng, S., Ding, Z., Zhang, G., 2016. Seismic tomography and anisotropy of the Helan-Liupan tectonic belt: Insight into lower crustal flow and seismotectonics. *J. Geophys. Res.-Solid.* Earth. 121, 2608–2635. https://doi.org/10.1002/2015JB012692.

Chiarabba, C., Chiodini, G., 2013. Continental delamination and mantle dynamics drive topography, extension and fluid discharge in the Apennines. Geology. 41 (6), 715–718. https://doi.org/10.1130/G33992.1.

Christensen, N.I., 1996. Poisson's ratio and crustal seismology. J. Geophys. Res. 101, 3139–3156. https://doi.org/10.1029/95JB03446.

Christensen, N.I., Mooney, W.D., 1995. Seismic velocity structure and composition of the continental crust: a global view. J. Geophys. Res.-Solid Earth 100, 9761–9788. https://doi.org/10.1029/95JB00259.

Ciotoli, G., Guerra, M., Lombardi, S., Vittori, E., 1998. Soil gas survey for tracing seismogenic faults: a case study in the Fucino Basin, Central Italy. J. Geophys. Res.-Solid Earth 103 (B10), 23781–23794. https://doi.org/10.1029/98JB01553.

Deng, Q.D., Zhang, P.Z., Ran, Y.K., Yang, X.P., Min, W., Chu, Q.Z., 2003. Basic characteristics of active tectonics of China. *Sci. China*. Ser. D-Earth Sci. 46, 356–372.

Etiope, G., Schoell, M., Hosgörmez, H., 2011. Abiotic methane flux from the Chimaera seep and Tekirova ophiolites (Turkey): Understanding gas exhalation from low temperature serpentinization and implications for Mars. Earth Planet. Sci. Lett. 310 (1–2), 96–104. https://doi.org/10.1016/j.epsl.2011.08.001.

Fu, C.C., Yang, T.F., Chen, C.H., Lee, L.C., Wu, Y.M., Liu, T.K., Walia, V., Kumar, A., Lai, T.H., 2017. Spatial and temporal anomalies of soil gas in northern Taiwan and its tectonic and seismic implications. J. Asian Earth Sci. 149, 64–77. https://doi.org/10.1016/j.jseaes.2017.02.032.

Graham, D.W., 2002. 2002. Noble Gas Isotope Geochemistry of Mid-Ocean Ridge and Ocean Island Basalts: Characterization of Mantle Source Reservoirs. In: Porcelli, D., Ballentine, C.J., Wieler, R. (Eds.), Noble Gases in Geochemistry and Cosmochemistry. Mineralogical Society of America, Washington, D C August, Reviews in Mineralogy and Geochemistry, pp. 247–318.

Hou, Y., Wang, Y., Zhang, G., 1994. A preliminary study of the influence factor on soil gas Radon measurement. North China Earthquake Sci. 12 (2), 55–59 (in Chinese with an English abstract).

Huang, Z., Tilmann, F., Xu, M., Wang, L., Ding, Z., Mi, N., Yu, D., Li, H., 2017. Insight into NE Tibetan Plateau expansion from crustal and upper mantle anisotropy revealed by shear-wave splitting. Earth Planet. Sci. Lett. 478, 66–75. https://doi.org/10.1016/j.epsl.2017.08.030.

Ingebritsen, S., Gleeson, T., 2017. Crustal permeability. Hydrogeol. J. 25 (8), 2221–2224. https://doi.org/10.1007/s10040-017-1663-4.

Jiang, G., Hu, S., Shi, Y., Zhang, C., Wang, Z., Hu, D., 2019. Terrestrial heat flow of continental China: Updated dataset and tectonic implications. Tectonophysics. 753, 36–48. https://doi.org/10.1016/j.tecto.2019.01.006.

Klemperer, S.L., 2006. Crustal flow in Tibet: geophysical evidence for the physical state of Tibetan lithosphere, and inferred patterns of active flow. Geol. Soc. Lond., Spec. Publ. 268, 39–70. https://doi.org/10.1144/GSL.SP.2006.268.01.03.

Kusky, T.M., Polat, A., Windley, B.F., Burke, K.C., Dewey, J.F., Kidd, W.S.F., Maruyama, S., Wang, J.P., Deng, H., Wang, Z.S., Wang, C., Fu, D., Li, X.W., Peng, H. T., 2016. Insights into the tectonic evolution of the North China craton through comparative tectonic analysis: a record of outward growth of Precambrian continents. Earth-Sci. Rev. 162, 387–432. https://doi.org/10.1016/j.earscirev.2016.09.002.

Lei, J.S., Zhao, D.P., 2016. Teleseismic P-wave tomography and mantle dynamics beneath Eastern Tibet. Geochem. Geophys. Geosyst. 17, 1861–1884. https://doi.org/10.1002/2016GC006262.

Li, Y., Wu, Q., Zhang, F., Feng, Q., Zhang, R., 2011. Seismic anisotropy of the Northeastern Tibetan Plateau from shear wave splitting analysis. Earth Planet. Sci. Lett. 304, 147–157. https://doi.org/10.1016/j.epsl.2011.01.026.

Li, J., L, Y., Lu, L., Sun, F., Xie, C., Cui, Y., 2017. Geochemistry of spring water in the Liupanshan Mountain area. Earthquake 37, 61–72 (in Chinese with an English abstract). https://doi.org/10.3969/j.issn.1000-3274.2017.01.007.

Li, Y., Liu, M., Wang, Q., Cui, D., 2018. Present-day crustal deformation and strain transfer in northeastern Tibetan Plateau. Earth Planet. Sci. Lett. 487, 179–189. https://doi.org/10.1016/j.epsl.2018.01.024.

Liu, K., Gao, S., Gao, Y., Wu, J., 2008. Shear wave splitting and mantle flow associated with the deflected Pacific slab beneath Northeast Asia. J. Geophys. Res.-Solid Earth 113, B01305. https://doi.org/10.1029/2007jb005178.

Molnar, P., England, P., Martinod, J., 1993. Mantle dynamics, uplift of the Tibetan Plateau, and the Indian Monsoon. Rev. Geophys. 31, 357–396. https://doi.org/10.1029/93rg02030.

O'Connell, R.J., Budiansky, B., 1974. Seismic velocities in dry and saturated cracked solids. J. Geophys. Res. 79, 5412–5426. https://doi.org/10.1029/JB079i035p05412.

Randazzo, P., Caracausi, A., Aiuppa, A., Cardellini, C., Chiodini, G., D'Alessandro, W., Li Vigni, L., Papic, P., Marinkovic, G., Ionescu, A., 2021. Active degassing of deeply sourced fluids in Central Europe: New evidences from a geochemical study in Serbia. Geochem. Geophys. Geosyst. 22 https://doi.org/10.1029/2021GC010017 e2021GC010017.

Rong, Y., Eeri, M., Xu, X., Cheng, J., Chen, G., Magistrale, H., Eeri, M., Shen, Z.K., 2020. A probabilistic seismic hazard model for mainland China. Earthquake Spectra 1–29. https://doi.org/10.1177/8755293020910754.

Royden, L.H., Burchfiel, B.C., van der Hilst, R.D., 2008. The geological evolution of the Tibetan Plateau. Science. 321, 1054–1058. https://doi.org/10.1126/science.1155371.

Sano, Y., Wakita, H., 1985. Geographical distribution of $^3He/^4He$ ratios in Japan: Implications for arc tectonics and incipient magmatism. J. Geophys. Res.-Solid Earth 90 (B10), 8729–8741. https://doi.org/10.1029/JB090iB10p08729.

Shao, Z.G., Wu, Y.Q., Ji, L.Y., Diao, F.Q., Shi, F.Q., Li, Y.J., Long, F., Zhang, H., Zhu, L.Y., Chen, C.Y., Wang, W.X., Wei, W.X., Wang, P., Liu, X.X., Liu, Q., Pan, Z.Y., Yin, X.F., Liu, Y., Feng, W., Zou, Z.Y., Cao, J.L., Xu, J., Han, L.B., Cheng, J., Lu, R.Q., Xu, Y.R., Li, X., Sun, X.Z., 2022. Comprehensive determination for the late stage of the interseismic period of major faults in the boundary zone of active tectonic blocks in Chinese mainland, China. J. Geophys. (in Chinese) 65 (12), 4643–4658 (in Chinese with an English abstract). https://doi.org/10.6038/cjg2022P0489.

Sun, A., Zhao, D., 2020. Anisotropic tomography beneath Northeast Tibet: evidence for regional crustal flow. Tectonics. 39 https://doi.org/10.1029/2020TC006161 e2020TC006161.

Sun, X., Wang, G., Shao, Z., Si, X., 2016. Geochemical characteristics of emergent gas and groundwater in Haiyuan fault zone. Earth Sci. Front. 23 (3), 140–150 (in Chinese with an English abstract). 10.13745/j.esf.2016.03.018.

Sun, A., Zhao, D., Gao, Y., Tian, Q., Liu, N., 2019. Crustal seismic imaging of Northeast Tibet using first and later phases of earthquakes and explosions. Geophys. J. Int. 217, 405–421. https://doi.org/10.1093/gji/ggz031.

Sun, A., Zhao, D., Guo, H., 2021. Cracks and fluids in the Northeast Tibetan crust: New insight into seismotectonics. Phys. Earth Planet. Inter. 311, 106634 https://doi.org/10.1016/j.pepi.2020.106634.

Tamburello, G., Pondrelli, S., Chiodini, G., Rouwet, D., 2018. Global-scale control of extensional tectonics on CO_2 earth degassing. Nat. Commun. 9, 4608. https://doi.org/10.1038/s41467-018-07087-z.

Tian, X., Bai, Z., Klemperer, S.L., Liang, X., Liu, Z., Wang, X., Yang, X., Wei, Y., Zhu, G., 2021. Crustal-scale wedge tectonics at the narrow boundary between the Tibetan Plateau and Ordos block. Earth Planet. Sci. Lett. 554, 116700 https://doi.org/10.1016/j.epsl.2020.116700.

Vannoli, P., Martinelli, G., Valensise, G., 2021. The seismotectonic significance of geofluids in Italy. Front. Earth Sci. 9, 579390 https://doi.org/10.3389/feart.2021.579390.

Wang, W.H., 2008. The study of the relationship between the characteristics of the deep fluid and the regional seismic activity in the Northern margin Fault Zone of the Qinling, (Master's thesis). In: Retrieved from China National Knowledge Infrastructure. (https://www.cnki.net/). Lanzhou Institute of Seismology, Lanzhou (in Chinese with an English abstract).

Wang, F., Zhang, B., 1991. The relation between the contents of rare-gases and trace-elements in hot springs and tectonic activities in the eastern Gansu province. Northwestern Seismological J. 13, 14–21 (in Chinese with an English abstract).

Wang, H., Liu, M., Cao, J., Shen, X., Zhang, G., 2011. Slip rates and seismic moment deficits on major active faults in mainland China. J. Geophys. Res. 116, B02405. https://doi.org/10.1029/2010JB007821.

Wei, W., Unsworth, M., Jones, A., Booker, J., Tan, H., Nelson, D., Chen, L., Li, S., Solon, K., Bedrosian, P., 2001. Detection of widespread fluids in the Tibetan crust by magnetotelluric studies. Science. 292, 716. https://doi.org/10.1126/science.1010580.

Xu, G., 2014. Isotope and hydrochemical evidence of genetic about deep geothermal water—as the central of Guanzhong basin for an example, (Master's thesis). In: Retrieved from China National Knowledge Infrastructure. (https://www.cnki.net/). Xi'an: Chang'an University (in Chinese with an English abstract).

Xu, X., Han, Z., Yang, X., Zhang, S., Yu, G., Zhou, B., Li, F., Ma, B., Chen, G., Ran, Y., 2016. Seismotectonic Atlas of China and its Vicinity. Earthquake Press, Beijing, China.

Ye, X., Wu, M., Sun, M., 2001. Determination of the noble gas isotopic composition in rocks and minerals by mass spectrometry. Rock Mineral Analysis 20, 174–178 (in Chinese with an English abstract).

Ye, X., Tao, M., Yu, C., Zhang, M., 2007. Helium and neon isotopic compositions in the ophiolites from the Yarlung Zangbo River, Southwestern China: the information from deep mantle. Sci. China Ser. D-Earth Sci. 50, 801–812. https://doi.org/10.1007/s11430-007-0017-9.

Yin, A., Harrison, T.M., 2000. Geologic evolution of the Himalayan-Tibetan orogen. Annu. Rev. Earth Pl. Sc. 28, 211–280. https://doi.org/10.1146/annurev.earth.28.1.211.

Yin, A., Rumelhart, P.E., Butler, R., Cowgill, E., Harrison, T.M., Foster, D.A., Ingersoll, R. V., Zhang, Q., Zhuo, X.Q., Wang, X.F., Hanson, A., Raza, A., 2002. Tectonic history of the Altyn Tagh fault system in northern Tibet inferred from Cenozoic sedimentation. Geol. Soc. Am. Bull. 114 (10), 1257–1295. https://doi.org/10.1130/0016-7606(2002)114<1257:thotat>2.0.co;2.

Zhan, Y., Yang, H., Zhao, G., Zhao, L., Sun, X., 2017. Deep electrical structure of crust beneath the Madongshan step area at the Haiyuan fault in the northeastern margin of the Tibetan plateau and tectonic implications. Chin. J. Geophys. 60, 2371–2384 (in Chinese with an English abstract).

Zhang, X., 2016. The characteristics of isotopes and hydrogeochemistry for geothermal water in the piedmont of Qinling Mountain—as Tangyu town in Lantian county for an example, (Master's thesis). In: Retrieved from China National Knowledge Infrastructure. (https://www.cnki.net/). Xi'an: Chang'an University (in Chinese with an English abstract).

Zhang, Y., Shi, W., Dong, S., 2019a. Neotectonics of North China: interplay between far-field effect of India-Eurasia collision and Pacific subduction related deep-seated mantle upwelling. Acta Geol. Sin. 93, 971–1001 (in Chinese with an English abstract). 10.19762/j.cnki.dizhixuebao.2019072.

Zhang, W., Li, Y., Zhao, F., Han, W., Li, Y., Wang, Y., Holland, G., Zhou, Z., 2019b. Using noble gases to trace groundwater evolution and assess helium accumulation in Weihe Basin, Central China. Geochim. Cosmochim. Acta 251, 229–246. https://doi.org/10.1016/j.gca.2019.02.024.

Zhao, D., Mizuno, T., 1999. Crack density and saturation rate in the 1995 Kobe earthquake region. Geophys. Res. Lett. 26, 3213–3216. https://doi.org/10.1029/1999GL005411.

Zhao, D., Kanamori, H., Negishi, H., Wiens, D., 1996. Tomography of the source area of the 1995 Kobe earthquake: evidence for fluids at the hypocenter? Science. 274, 1891–1894. https://doi.org/10.1126/science.274.5294.1891.

Zhao, G., Tang, J., Zhan, Y., Chen, X., Zhuo, X., Wang, J., Xuan, F., Deng, Q., Zhao, J., 2005. Relation between electricity structure of the crust and deformation of crustal blocks on the northeastern margin of Qinghai-Tibet Plateau. *Sci. China*. Ser. D: Earth Sci. 48, 1613–1626.

Zhao, P., Chen, J., Li, Y., Liu, Q., Chen, Y., Guo, B., Yin, X., 2021. Growth of the northeastern Tibetan Plateau driven by crustal channel flow: evidence from high-resolution ambient noise imaging. Geophys. Res. Lett. 48 (13) https://doi.org/10.1029/2021GL093387 e2021GL093387.

Zhou, X., Wang, W., Chen, Z., Yi, L., Liu, L., Xie, C., Cui, Y., Du, J., Cheng, J., Yang, L., 2015. Hot spring gas geochemistry in western Sichuan Province, China after the Wenchuan M_S 8.0 earthquake. Terr. Atmos. Ocean. Sci. 26 (4), 361–373.